Rich topological spin textures in single-phase and core-shell magnetic nanodisks

Sen Li,[1] Qinyun Li,[1] Jiancheng Liu,[1] Nian Ran,[1] Ping Lai,[2,*] Laichuan Shen,[3] Jing Xia,[1,6] Linhua Xie,[1,4] Yan Zhou,[5,†] and Guoping Zhao[1,6,‡]

[1]*College of Physics and Electronic Engineering, Sichuan Normal University, Chengdu 610068, China*
[2]*School of Electronic Information and Automation, Aba Teachers University, Wenchuan 623002, China*
[3]*The Center for Advanced Quantum Studies and Department of Physics, Beijing Normal University, Beijing 100875, China*
[4]*Institute of Solid State Physics, Sichuan Normal University, Chengdu 610066, China*
[5]*School of Science and Engineering, The Chinese University of Hong Kong, Shenzhen, Guangdong 518172, China*
[6]*Center for Magnetism and Spintronics, Sichuan Normal University, Chengdu 610068, China*

(Received 5 July 2022; revised 25 December 2022; accepted 3 January 2023; published 18 January 2023)

Magnetic skyrmions have potential applications in future high-density information storage devices due to their small size, topologically protected structure, and ultralow energy consumption. Here, we use a variational method to study rich topological spin textures in magnetic nanodisks, including skyrmions and skyrmionlike objects. The existence of skyrmions and $k\pi$-skyrmions in a single-phase nanodisk and a disk with a core-shell structure is investigated theoretically, where the phase diagrams of possible spin states are obtained for various Dzyaloshinskii-Moriya interaction (DMI) constants and disk dimeters. Our calculations suggest that skyrmions can be generated spontaneously in a core-shell nanodisk. We also study the transitions of spin textures in the nanodisk induced by spin currents. This paper may provide guidelines for experimental realization of different topological spin textures in nanodisks with certain DMIs. The simple two-dimensional analytical method used in this paper can be used to study the magnetic phase diagrams of thin films with interface-induced DMIs.

DOI: 10.1103/PhysRevB.107.014414

I. INTRODUCTION

The concept of a skyrmion was initially proposed as a model for hadrons [1], which has been extended to the field of magnetism and spintronics [2–4]. As particlelike magnetic configurations, skyrmions have potential applications in future data storage and processing devices [5–15] due to their excellent properties such as the nanoscale size and ultralow power consumption [9,16–19]. Specifically, magnetic skyrmions can be used in racetrack memories [20–23], logic gates [24–27], transistorlike devices [28,29], diodes [30], nano-oscillators [31,32], and neuromorphic computing devices [33,34]. Therefore, it is crucial to find different skyrmionlike spin structures in magnetic materials. For example, ferromagnetic (FM) skyrmions [35–42], antiferromagnetic skyrmions [43–46], antiskyrmions [47,48], biskyrmions [49,50], and skyrmioniums [51–58] have been found in a wide variety of magnetic materials and nanostructures, which have aroused significant interest recently.

Apparently, the creation and stabilization of skyrmions and skyrmionlike states are important for skyrmion-based applications. Skyrmions can be created and remain stable in magnetic films with the Dzyaloshinskii-Moriya interaction (DMI) [5,9]. To be specific, Bloch-type skyrmions are observed in B20 chiral magnets like MnSi, FeGe, Cu_2OSeO_3, and $Fe_{1-x}Co_xSi$ [35–40], in which the bulk DMIs come from the broken inversion symmetry by the atomic structures. On the other hand, Néel-type skyrmions are found in ultrathin FM/heavy metal films with interface-induced DMIs [8,9,59,60]. In addition, Boulle *et al.* [61] have generated stable skyrmions in sputtered ultrathin Pt/Co/MgO multilayers at room temperature with zero external magnetic field and a small DMI value. However, there are still few reports of generating and stabilizing skyrmions in complex magnetic nanostructures, such as core-shell nanostructures. These nanostructures can combine different functionalities of both core and shell, which might improve magnetic properties while exhibiting rich physics.

With the development of synthetic chemistry, researchers can produce more advanced magnetic nanosamples comprising two (or more) materials such as core-shell nanodisks [62] and nanowires [63]. These types of multiphase nanostructures have extensive applications in various fields (e.g., catalytical, optical, magnetic, or biomedical) because they can combine the different functionalities of the diverse constituents bringing about enhanced properties [64]. For certain applications, the use of bimagnetic core/shell structure materials can be advantageous over single-phase magnetic materials. It has been shown theoretically that skyrmions can be formed in exchange-coupled core (Co)-shell (Pt/Co) nanodisks [62].

In this paper, we use a variational method to study rich topological spin textures in both single-phase and core-shell nanodisks. It is found that a $k\pi$-skyrmion will be formed if the DMI or the radius of the disk is large enough, which is composed of multiple circular domain walls. In these structures, the magnetization direction rotates by an angle of $k\pi$ between

*laipingiu@163.com
†zhouyan@cuhk.edu.cn
‡zhaogp@uestc.edu.cn

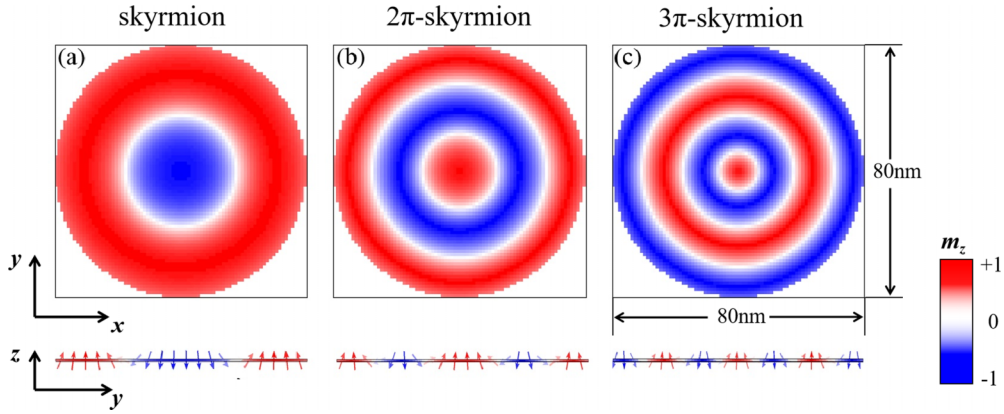

FIG. 1. Top view (seen from the $+z$ direction) and side view (seen from the y-z plane) of various Néel-type skyrmions: (a) a skyrmion with the inner and outer domains orienting up and down, respectively; (b) a 2π-skyrmion; and (c) a 3π-skyrmion. The red and blue colors denote the positive and negative domains, respectively, where the z component of the magnetization is indicated by the color scale.

the center and the FM background. The spin configurations in Figs. 1(b) and 1(c) are called 2π- and 3π-skyrmions, respectively. Similarly, the spin structure in Fig. 1(a) is called a typical Néel-type skyrmion [8]. It is noted that the transition from the skyrmion to $k\pi$-skyrmions [54] is analogous to the transformation from the single-domain grain to a multidomain grain. As the grain size increases, the magnetostatic energy dominates over the exchange energy so that it is more favorable to form multiple domains in a single grain. Here, it is the DMI which is the main influence factor driving force to change the spin configuration from a FM state to a skyrmion and finally to a $k\pi$-skyrmion.

Such a 2π-skyrmion has been observed experimentally on a TbFeCo film by laser radiation [53,54], which is referred to as a skyrmionium in some literature [51,52,55–58]. Theoretical demonstrations of 2π-skyrmions or even 3π-skyrmions have been made recently, which suggest that $k\pi$-skyrmions may have some advantages over the conventional skyrmions [56–58]. Skyrmioniums and other higher-order skyrmions with $Q = 0$ will not suffer from skyrmion Hall effects when they are driven by currents due to their zero topological number [57]. However, it remains elusive regarding the formal extensions of skyrmions from two-domain spin-structures to multidomain ones.

In this paper, both analytical and numerical micromagnetic calculations are adopted to investigate various topological spin structures created in magnetic nanodisks. We find that $k\pi$-skyrmions are more common spin structures which can occur naturally for a sufficiently large DMI or host size, even in the ground state. In the absence of external stimulus, skyrmions, which require lower DMI values, as well as $k\pi$-skyrmions, can be formed spontaneously in the core-shell structures.

II. TWO-DIMENSIONAL VARIATIONAL METHODS AND THREE-DIMENSIONAL MICROMAGNETIC SIMULATIONS

A continuous variational method [65,66] is adopted in this paper to calculate the total energy of various spin structures in a single-phase nanodisk or a disk with a core-shell structure. Direct analytical calculation is impossible, as the spin structure is generally a three-dimensional (3D) one. Considering that both nanodisks and skyrmion solutions have rotational symmetry, a cylindrical coordinate, as shown in Fig. 2, is used in this paper.

The thickness of the disk is very small (only 0.4 nm) so that the spin orientation θ only varies with r, where r is the distance from the center of the nanodisk to anywhere on the nanodisk, and the angle θ is referenced from the $+z$ direction [67]. The Bloch-type skyrmion occurs in the presence of the bulk DMI, in contrast to the Néel-type skyrmion, which appears with an interfacial DMI. In the continuous micromagnetic model, the average energy density for the bulk DMI reads

$$\begin{aligned} f_D &= -D[\mathbf{m}\cdot(\nabla\times\mathbf{m})] \\ &= D\left(m_z\frac{\partial m_x}{\partial y} - m_x\frac{\partial m_z}{\partial y} - m_z\frac{\partial m_y}{\partial x} + m_y\frac{\partial m_z}{\partial x}\right) \\ &= -D\left[\frac{\cos\theta\sin\theta\,\sin(\alpha-\varphi)}{r} + \cos\theta\sin\theta\cos(\alpha-\varphi)\alpha_r\right. \\ &\quad \left. + \frac{\cos\theta\sin\theta\cos(\alpha-\varphi)(\alpha_\varphi-1)}{r} + \sin(\alpha-\varphi)\theta_r\right]. \end{aligned} \tag{1}$$

Here, D is the DMI constant, $\mathbf{m}$ is the magnetization vector, $\alpha_r = d\alpha/dr$, $\alpha_\varphi = d\alpha/d\varphi$, and $\theta_r = d\theta/dr$. In contrast to the interfacial DMI, the average energy density can be read as

$$\begin{aligned} f_D &= D[m_z(\mathbf{m}\cdot\nabla) - (\nabla\cdot\mathbf{m})m_z] \\ &= D\left(m_z\frac{\partial m_x}{\partial x} - m_x\frac{\partial m_z}{\partial x} + m_z\frac{\partial m_y}{\partial y} - m_y\frac{\partial m_z}{\partial y}\right) \\ &= -D\left[\frac{\cos\theta\sin\theta\,\cos(\alpha-\varphi)}{r} - \cos\theta\sin\theta\sin(\alpha-\varphi)\alpha_r\right. \\ &\quad \left. + \frac{\cos\theta\sin\theta\cos(\alpha-\varphi)(\alpha_\varphi-1)}{r} + \cos(\alpha-\varphi)\theta_r\right]. \end{aligned} \tag{2}$$

For the Bloch-type skyrmion, $\alpha-\varphi = \pi/2$, $\alpha_\varphi = 1$, and $\alpha_r = 0$. Thus, the average energy density for the bulk DMI

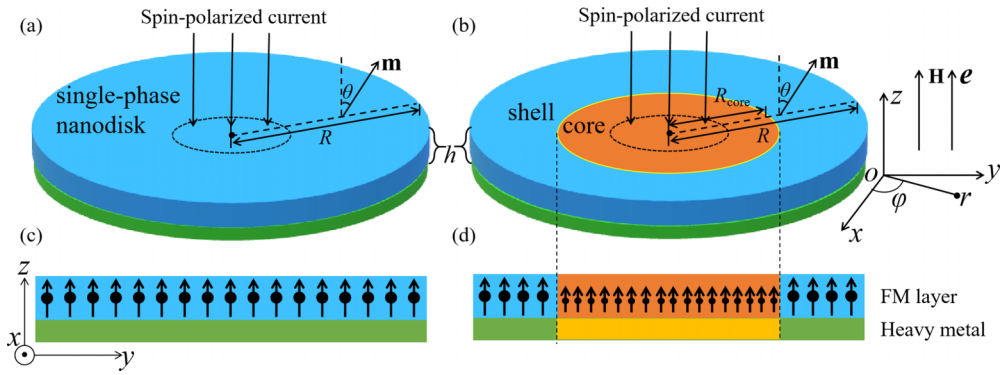

FIG. 2. Schematic of the (a) and (c) single-phase and (b) and (d) core-shell nanodisk. (a) and (b) Front view: The blue area represents the ferromagnetic (FM) layer, and for the core-shell structure, the orange and blue areas represent the core and shell parts, respectively. R, R_{core}, and h represent the total radius, the radius of the core region, and the thickness of the nanodisk, respectively. r is the distance from the center of the nanodisk to anywhere of the nanodisk, and θ represents the angle between the magnetization vector **m** and the $+z$ direction. The direction of the applied field **H** and the magnetocrystalline anisotropy easy axis **e** are along the $+z$ direction. The region surrounded by the black dotted line is the region where the spin-polarized current is injected. (c) and (d) Side view: The top layer is a FM material, and the bottom layer is a heavy metal. The bottom heavy metal layer of core-shell structure is used to produce DMIs of different strength.

with a Bloch-type skyrmion can be rewritten as

$$f_D = -D[\mathbf{m}\cdot(\nabla\times\mathbf{m})] = -D\left[\frac{d\theta}{dr}+\frac{\cos\theta\sin\theta}{r}\right]. \quad (3)$$

In contrast, for the Néel-type skyrmion, $\alpha-\varphi=0$, $\alpha_\varphi=1$, and $\alpha_r=0$. Therefore, the average energy density for the interfacial DMI with a Néel-type skyrmion can be rewritten as

$$\begin{aligned} f_D &= -D[m_z(\nabla\cdot\mathbf{m})-(\mathbf{m}\cdot\nabla)m_z] \\ &= -D\left[\frac{d\theta}{dr}+\frac{\cos\theta\sin\theta}{r}\right], \end{aligned} \quad (4)$$

which is the same as the average energy density for the bulk DMI with a Bloch-type skyrmion. Therefore, the total free energy of a Bloch-type skyrmion in a single-phase nanodisk is equal to that of the Néel type. It should be noted that the energy of the Néel-type skyrmion is slightly larger than that of the Bloch type due to the volume magnetostatic charges, according to our simulation. However, we used the shape anisotropy to approximate the magnetostatic energy in our analytical calculation, where the volume magnetostatic charges are ignored. As a result, the energy of a Bloch-type skyrmion is the same as that of the Néel type according to our formula. Then the total free energy of a skyrmion in a single-phase nanodisk can be written as [67]

$$\begin{aligned} E = 2\pi h\int_0^R f r dr = 2\pi h\int_0^R \Bigg\{ & A\left[\left(\frac{d\theta}{dr}\right)^2+\frac{\sin^2\theta}{r^2}\right] \\ & - D\left(\frac{d\theta}{dr}+\frac{\sin\theta\cos\theta}{r}\right)+K\sin^2\theta \\ & + \frac{1}{2}\mu_0 M_S^2\cos^2\theta-\mu_0 H M_S\cos\theta\Bigg\} r dr, \end{aligned} \quad (5)$$

where R and h denote the radius and thickness of the nanodisk, respectively. Here, f, A, K, M_S, and H are the total energy density, the exchange stiffness, the perpendicular magnetic anisotropy constant (i.e., the easy axis points to the $+z$ direction), the saturation magnetization, and the applied field amplitude, respectively. The five terms at the right-hand side of Eq. (5) correspond to the exchange energy, the DMI energy, the anisotropy energy, the magnetostatic energy, and the Zeeman energy, respectively. The Bloch-type skyrmions can be calculated similarly. After such simplifications, an analytical variational method can be carried on.

Using standard variation calculus, we could get

$$\delta E = 2\pi h\int_0^R\left\{\frac{\partial(rf)}{\partial\theta}-\frac{\partial}{\partial r}\left[\frac{\partial(rf)}{\partial\left(\frac{d\theta}{dr}\right)}\right]\right\}\delta\theta dr = 0, \quad (6a)$$

$$\left[\frac{\partial(rf)}{\partial\left(\frac{d\theta}{dr}\right)}\delta\theta\right]_{\theta(0)}^{\theta(R)} = 0. \quad (6b)$$

Due to the arbitrary value of $\delta\theta$, Eq. (6a) requires the following equation to hold:

$$F[\theta(r)] = \frac{\partial(rf)}{\partial\theta}-\frac{\partial}{\partial r}\left[\frac{\partial(rf)}{\partial\left(\frac{d\theta}{dr}\right)}\right] = 0, \quad (7)$$

where

$$\frac{\partial(rf)}{\partial\left(\frac{d\theta}{dr}\right)} = r\left(2A\frac{d\theta}{dr}-D\right), \quad (8a)$$

$$\frac{\partial(rf)}{\partial\theta} = r\left(\frac{A\sin2\theta}{r^2}-D\frac{\cos2\theta}{r}+K_{\text{eff}}\sin2\theta-\mu_0 H M_S\sin\theta\right). \quad (8b)$$

Thus,

$$\begin{aligned} F[\theta(r)] = & \frac{d^2\theta}{dr^2}+\frac{1}{r}\frac{d\theta}{dr}-\left(\frac{1}{r^2}+\frac{2K-\mu_0 M_S^2}{2A}\right)\sin\theta\cos\theta \\ & - D\frac{\sin^2\theta}{Ar}-\frac{\mu_0 H M_S\sin\theta}{2A}. \end{aligned} \quad (9)$$

Equation (9) describes the variation of θ in the nanodisk. It must be integrated numerically with the initial value $\theta(r=0)=0$. Solving Eq. (9) with the following boundary

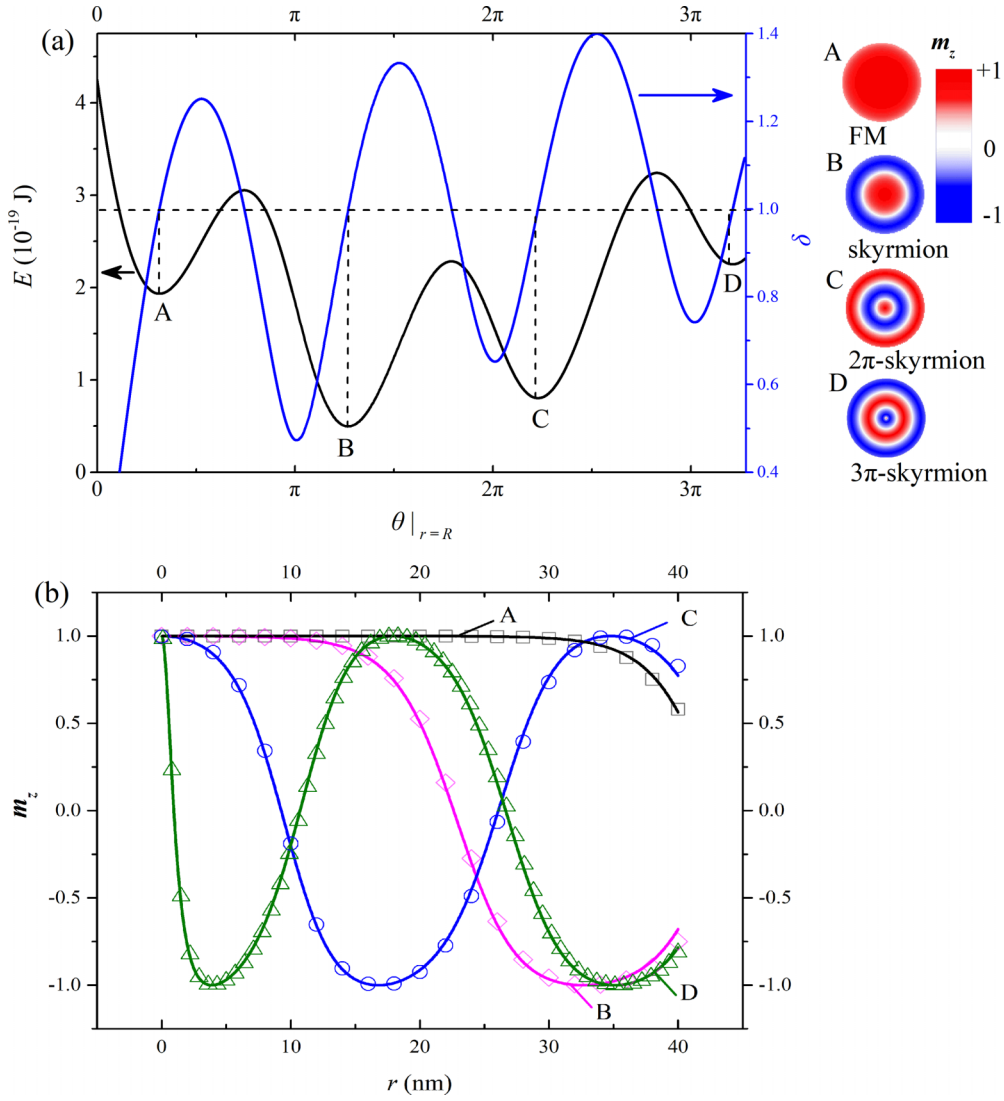

FIG. 3. (a) Calculated total energy for different spin structures with DMI constant $D = 5\,\mathrm{mJ/m^2}$ and $R = 40\,\mathrm{nm}$ in a single-phase nanodisk, where $\theta|_{r=R}$ stands for the spin orientation at the disk edge. Points A–D denote four energy minima in the total energy curve, corresponding to the ferromagnet (FM), skyrmion, 2π-skyrmion, and 3π-skyrmion states, respectively. The boundary condition is calculated to ensure the reliability of the energy minimization. δ equals exactly 1 at points A–D, indicating that the boundary condition is well satisfied at the four energy minimum states, where $\delta = (d\theta/dr)/(D/2A)$. (b) Calculated radial variation for the out-of-plane spin component m_z for the four kinds of spin structures indicated by points A–D in (a). The open symbols are the results of numerical calculations for comparison with analytical results. The color scale shows the out-of-plane component of magnetization m_z.

conditions [67] gives the spin orientation in the radial direction of the nanodisk:

$$\cos\theta = \pm 1 \quad \text{for } r = 0, \tag{10a}$$

$$\frac{d\theta}{dr} = \frac{D}{2A} \quad \text{for } r = R. \tag{10b}$$

The former is the Dirichlet boundary condition [67], which sets the orientation of the magnetization at the center, while the latter is the free boundary condition. Utilizing the above equations and boundary conditions, we can obtain the energy minima where the corresponding states are stable. The magnetic parameters for CoPt nanodisk for the present calculation are adopted from Refs. [16,17,20]: the saturation magnetization $M_S = 580\,\mathrm{kA/m}$, the exchange stiffness $A = 15\,\mathrm{pJ/m}$, and the crystalline anisotropy constant $K = 0.8\,\mathrm{MJ/m^3}$. In our calculation, Eq. (6b) leads to the natural boundary condition in Eq. (10b), which is used to calculate the energy curves, as illustrated in Fig. 3. The initial value for $d\theta/dr$ $(r = 0)$ is adjusted to fulfill the boundary condition (shooting method). It is found that, only at the energy minima and maxima, the condition in Eq. (10b) is well satisfied, justifying our calculation.

The same method can be applied to a magnetic disk with a core-shell structure and extended to other types of spin structures such as a Bloch-type skyrmion or a vortex in a nanodisk. Two basic assumptions have been made in here. The first is that the magnetostatic interactions between the core and shell region are ignored (see Appendix A). The second is that, at the interface, each atom of a given phase is assumed to interact only with the (nearest neighbor) atom of the facing atomic

plane belonging to the other phase. Thus, in the core-shell structure, the total free energy of a skyrmion can be written as

$$E = E_{\text{core}} + E_{\text{shell}} - 2\pi R_{\text{core}} hJ[\cos(\theta_{\text{core}} - \theta_{\text{shell}}) - 1], \tag{11}$$

where E_{core} and E_{shell} represent the total free energy of a skyrmion in the core ($0 < r \leqslant R_{\text{core}}$) and in the shell ($R_{\text{core}} < r \leqslant R$), respectively, given by Eq. (5). Here, R_{core} and R denote the radius of the core and the total radius of the disk, respectively. Also, J represents the interface exchange coupling constant, and $\theta_{\text{core}} - \theta_{\text{shell}}$ denotes the difference of the spin orientations at the interface between the core and the shell. In this paper, we consider the case of the strong interface coupling, which leads to $\theta_{\text{core}}(r) = \theta_{\text{shell}}(r)$ at $r = R_{\text{core}}$, and hence, the last term in Eq. (11) can be disregarded.

Similarly, a variation of Eq. (11) yields the following equation for $\theta(r)$:

$$F_{\text{core}}[\theta(r)] = 0 \quad \text{for } r \leqslant R_{\text{core}}, \tag{12a}$$

$$F_{\text{shell}}[\theta(r)] = 0 \quad \text{for } R_{\text{core}} < r \leqslant R. \tag{12b}$$

Solving Eqs. (12a) and (12b) with the following boundary conditions gives the spin orientation in the radial direction of the core-shell nanodisk:

$$\cos\theta = \pm 1 \quad \text{for } r = 0, \tag{13a}$$

$$2A_{\text{shell}}\frac{d\theta}{dr} - D_{\text{shell}} = 0 \quad \text{for } r = R, \tag{13b}$$

$$2A_{\text{core}}\frac{d\theta}{dr} - D_{\text{core}} = \left(2A_{\text{shell}}\frac{d\theta}{dr} - D_{\text{shell}}\right) \quad \text{for } r = R_{\text{core}}. \tag{13c}$$

Utilizing the above equations and the boundary conditions, we can obtain the energy minima where the corresponding states are stable in the core-shell nanodisk.

The variational methods presented above are general, which can be used to study spin structures in various composite magnetic materials and provide guidelines for storage and logic device design. In this paper, we focus on the effects of the DMI and saturation magnetization so that only these two parameters in the shell are different from those of the core.

The 3D micromagnetic simulations are performed using OOMMF [68] including the extension module for the interface-induced DMI [69] in a core-shell nanodisk ($R = 40$ nm) with thickness $h = 0.4$ nm. The magnetization dynamics is controlled by the Landau-Lifshitz-Gilbert equation [70,71], having the antidampinglike spin-transfer torque [69]:

$$\frac{d\mathbf{m}}{dt} = -\gamma_0 \mathbf{m} \times \mathbf{H}_{\text{eff}} + \alpha\left(\mathbf{m} \times \frac{d\mathbf{m}}{dt}\right) - \frac{\gamma_0 \hbar j P}{2\mu_0 e h M_s}[\mathbf{m} \times (\mathbf{m} \times \mathbf{m}_p)], \tag{14}$$

where $\mathbf{m} = \mathbf{M}/M_S$ is the reduced magnetization, t denotes the time, while j is the current density, α is the Gilbert damping coefficient, γ_0 is the gyromagnetic ratio, and P is the spin Hall angle. The effective field $\mathbf{H}_{\text{eff}}$ is expressed as follows:

$$\mathbf{H}_{\text{eff}} = -\frac{1}{\mu_0}\frac{\delta E}{\delta \mathbf{M}}. \tag{15}$$

In the above equation, the average energy density E [72] is a function of $\mathbf{M}$ specified by

$$E = A\left[\nabla\left(\frac{\mathbf{M}}{M_S}\right)\right]^2 - K\frac{(\mathbf{e}\cdot\mathbf{M})^2}{M_S^2} - \mu_0 \mathbf{M}\cdot\mathbf{H} - \frac{\mu_0}{2}\mathbf{M}\cdot\mathbf{H}_d(\mathbf{M}) + \frac{D}{M_S^2}\left(M_Z\frac{\partial M_x}{\partial x} + M_Z\frac{\partial M_y}{\partial y} - M_x\frac{\partial M_Z}{\partial x} - M_y\frac{\partial M_Z}{\partial y}\right), \tag{16}$$

where $\mathbf{H}$ and $\mathbf{H}_d$ ($\mathbf{M}$) are the applied and magnetostatic self-interaction fields, while $M_S = |\mathbf{M}(r)|$ is the saturation magnetization, and M_x, M_y, and M_z are the components of the magnetization $\mathbf{M}$. The five terms at the right side of Eq. (16) correspond to the exchange energy, the anisotropy energy, the applied field energy, the magnetostatic energy, and the DMI energy, respectively. A sufficiently small cell size of $1 \times 1 \times 0.4$ nm is used to achieve good numerical accuracy.

III. RESULTS

To study the possible nontrivial spin textures, we have carried out both analytical and micromagnetics calculations for the energy-favored spin distributions in CoPt nanodisks. The total energy for various skyrmion and FM states with DMI constant $D = 5\,\text{mJ/m}^2$ and disk size $R = 40$ nm have been calculated analytically and compared in Fig. 3(a), including the exchange energy, the DMI energy, the crystalline anisotropy energy, and the magnetostatic energy. Four energy minima occur in Fig. 3(a), corresponding to the FM state and three Néel-type skyrmions, i.e., 1π–3π-skyrmions, respectively. It should be noted that, for all four energy-minimum states, the calculated $\delta = 1$, indicating that the boundary condition $d\theta/dr = D/2A$ is well satisfied.

In this case, both skyrmion and 2π-skyrmion states have much lower energy than the FM state. However, the energy barriers exist between the FM and the skyrmion states [9,73] so that a certain load such as a spin current or a magnetic field is required to drive the spins to overcome the energy barrier for the formation of the skyrmion states [16]. We simulate the nucleation of the skyrmion by perpendicularly injecting a spin-polarized current in a circular region. Our numerical calculation shows that a minimum spin current of $1.9 \times 10^{12}\,\text{A/m}^2$ is needed to create a skyrmion, while a spin current of $3.6 \times 10^{12}\,\text{A/m}^2$ is necessary for a 2π-skyrmion to form in the nanodisk. Such methods have been adopted by various groups as standard methods to create skyrmions in experiments [74] or to numerically nucleate skyrmions in nanodisks [16,75,76] and nanotracks [9,17].

The spin distributions have also been calculated analytically and shown in Fig. 3(b), where the spin component perpendicular to the disk plane is illustrated. One can see that the spin angle encounters $\sim \frac{1}{2}$, 1, and $\frac{3}{2}$ periods of change for 1π-, 2π-, and 3π-skyrmions, respectively. However, the orientation of the spin at the disk edge is not exactly perpendicular to the disk plane due to the DMI. Similar spin canting at the disk edge has been obtained by other groups, both in experiments [77] and in theory [44,57,67].

Such energy-based analyses have been carried out to find the possible stable states for other disk sizes and material parameters. Figure 4(a) shows the phase diagram of possible

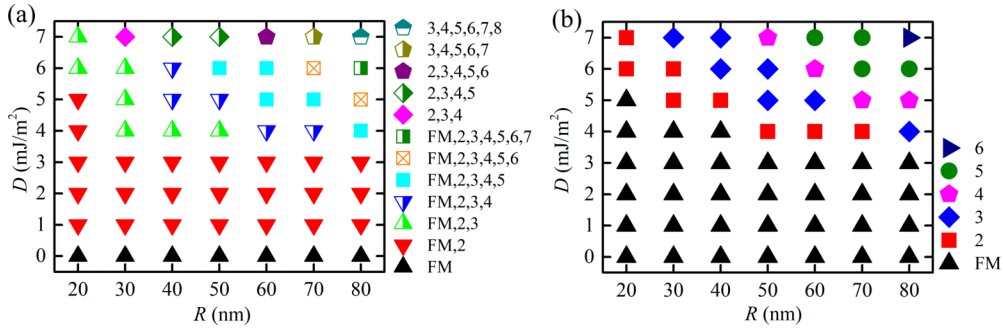

FIG. 4. Calculated phase diagram for the spin structures in a single-phase CoPt nanodisk with various DMI constants D and disk radii R. (a) The D-R phase diagram of the possibly stable states, where the total energy is a local minimum. (b) The D-R phase diagram of the ground state. As the DMI increases, the ground state of the spin structures changes from the ferromagnetic (FM) state to the skyrmion and finally to the $k\pi$-skyrmion. The numbers 2–8 represent the skyrmion states 1π–7π, respectively.

energy-minimized spin structures for various DMI constants D and disk radii R in zero field. When $D = 0\,\mathrm{mJ/m^2}$, only the FM state can exist, indicating that skyrmions are not stable states without the DMI. The skyrmion can occur for $1\,\mathrm{mJ/m^2} \leqslant D \leqslant 3\,\mathrm{mJ/m^2}$ along with the FM state at the adopted size region. Here, $k\pi$-skyrmions appear for larger D, where the number of the possible states increases with the disk size. The larger the value of D, the more domains for the skyrmions existent. Therefore, skyrmions can form spontaneously in the CoPt nanodisk. The disk size has a similar effect on the spin structures. When $D \geqslant 7\,\mathrm{mJ/m^2}$ and $R > 60$ nm, only $k\pi$-skyrmions can stably exist at the disk. As for the value of the DMI, the measured D values of the $[\mathrm{Pt/Co/Ta}]_n$ and $[\mathrm{Pt/Co/Ir}]_n$ [78,79] multilayer systems are $\sim 2.0\,\mathrm{mJ/m^2}$. Here, we adopted a large region for the value of the DMI, which changes from 0 to $7.0\,\mathrm{mJ/m^2}$ to see the important role played by the DMI in nucleating topological spin structures. Similar values of the DMI have been adopted by Sampaio *et al.* [16] and Rohart and Thiaville [67]. It should be noted that the DMI can also be controlled by the strain or the voltage [80,81] so that DMI values $>2.0\,\mathrm{mJ/m^2}$ can be possible. Nevertheless, the DMI value of $7.0\,\mathrm{mJ/m^2}$ is too large to be realized at the present time in experiment which, however, might be realized with the development of science and technology in the future.

One can see from Fig. 4(a) that, in most cases, there are a few stable spin structures in the disk, where at most eight types of structures can occur. Importantly, only one state has the lowest energy, i.e., the ground state. Figure 4(b) displays the phase diagrams of the ground states for various D and R. For a small DMI constant ($D \leqslant 3\,\mathrm{mJ/m^2}$), the FM state is the most stable at the adopted size region, whereas for a large DMI constant, skyrmion states are more energetically favored. When $D \geqslant 6\,\mathrm{mJ/m^2}$, the skyrmion is the ground state for small disk size, while the 4π-skyrmion (for $D = 6\,\mathrm{mJ/m^2}$) or the 5π-skyrmion (for $D = 7\,\mathrm{mJ/m^2}$) is the most stable for a large disk. Overall, the larger the values of D and R, the more domains for the skyrmions existent. The $k\pi$-skyrmions become the ground state when $R \geqslant 50$ nm for $D \geqslant 5\,\mathrm{mJ/m^2}$, indicating that these complicated spin structures are more common than FMs or skyrmions for sufficiently large DMIs.

The phase diagrams in Fig. 4 agree well with available experimental and theoretical results [16,56,57,60]. For example, Sampaio *et al.* [16] have nucleated the skyrmion and 2π-skyrmion in a nanodisk ($R = 40$ nm) in theory with various spin currents and DMIs based on the micromagnetic simulations, whereas only FM states are obtained for smaller DMI constants, in accordance with the ground states displayed in Fig. 4(b). However, it should be noted that the ground state is not the only state which can stably occur in the nanodisk. The

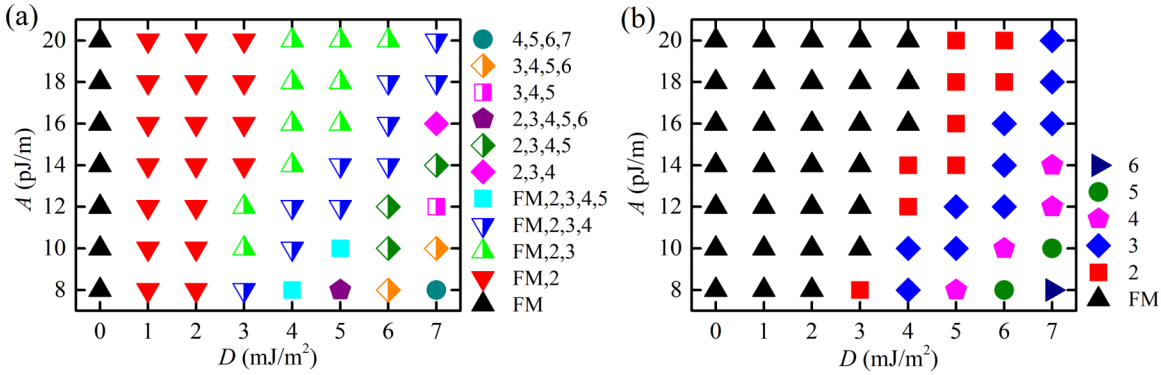

FIG. 5. Phase diagram for the spin structures in a single-phase CoPt nanodisk ($R = 40$ nm) with various exchange stiffnesses A and DMI constants D. (a) The A-D phase diagram of the possibly stable states, where the total energy reaches a local minimum. (b) The A-D phase diagram of the ground state. FM denotes the ferromagnetic state, and 2–7 represent skyrmion states 1π–6π, respectively.

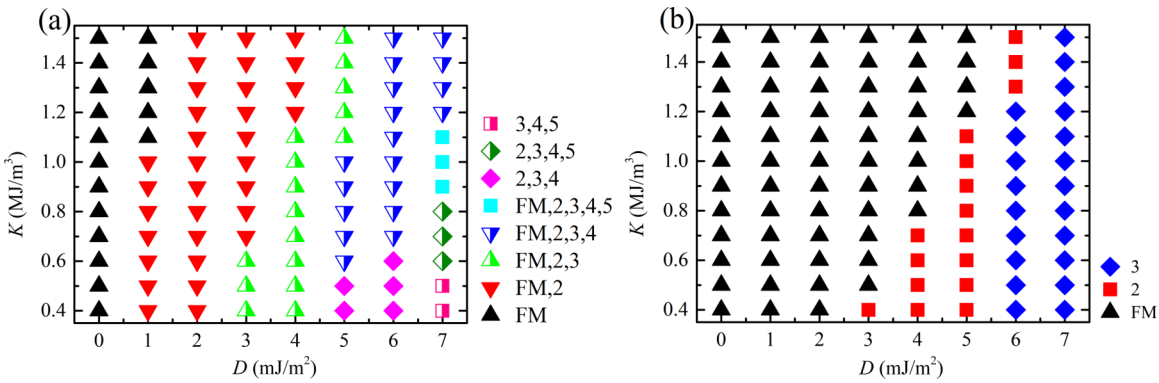

FIG. 6. Phase diagram for the spin structures in a single-phase CoPt nanodisk ($R = 40\,\text{nm}$) with various crystalline anisotropy constants K and DMI constants D. (a) The K-D phase diagram of the possibly stable states, where the total energy is a local minimum. (b) The K-D phase diagram of the ground state. As the DMI increases, the ground state of the spin structures changes from the ferromagnetic (FM) state to the skyrmion and finally to the 2π-skyrmion. Here, 2–5 represent skyrmion states 1π–4π, respectively.

excited states can exist stably due to the huge energy barriers between them, and the ground state depends on the initial magnetic configuration and the angle of the spin current. As D increases, more complex skyrmion states might occur. As shown in Fig. 4(b), 3π-skyrmions become the ground state when $70\,\text{nm} \leqslant R \leqslant 80\,\text{nm}$ at $D = 5\,\text{mJ/m}^2$. The same result has been obtained by the numerical work of Zhang *et al.* [57], where the 3π-skyrmion state is the most stable state when $4\,\text{mJ/m}^2 \leqslant D \leqslant 6\,\text{mJ/m}^2$ for $R = 75\,\text{nm}$. It is worth noting that our variational method presented in this paper can also yield some instructive results, which cannot be found by the commonly used numerical methods. One example is that the skyrmion state can possibly exist in the nanodisks with a wide range of R ($20\,\text{nm} \leqslant R \leqslant 80\,\text{nm}$) when $D = 1\,\text{mJ/m}^2$, shown in Fig. 4(a), where the DMI constant D is much smaller than that requested by other groups. Experimentally, it is found that the skyrmion state can be nucleated in CoPt systems with a DMI as low as $1.3\,\text{mJ/m}^2$ [60], agreeing well with our predictions.

The DMI constant and disk radius are not the only factors influencing the nucleation of spin structures; thus, we also calculated the A-D, K-D, and M_S-D phase diagrams, respectively, in a nanodisk with $R = 40\,\text{nm}$, as shown in Figs. 5–8 (see Appendixes B and C). One can see from Figs. 6 and 7 that the spin states are not sensitive to the value of exchange stiffness A and magnetic anisotropy K when D is small, especially for the ground state in Figs. 5(b) and 6(b). When the DMI constant is large, A and K have a relatively larger effect on the spin state, where the larger the values of A and K, the lower the probability for high-order skyrmion states. This trend is opposite to that of the saturation magnetization, where the larger the value of M_S, the higher the probability for higher-order skyrmion states. Physically, the phase diagram and the spin structure are affected by the saturation magnetization M_S mainly through the effective magnetic anisotropy K_{eff}. The larger the value of M_S, the lower the value of K_{eff}, and hence, the higher the probability for higher-order skyrmion states (see Appendix D).

It should be noted, however, although a skyrmion can be nucleated at a pure CoPt nanodisk with a DMI constant as small as $1\,\text{mJ/m}^2$, only at a sufficiently large DMI, skyrmions can exist spontaneously. To reduce the DMI constant to a more reasonable value, we design a core-shell structure which can produce skyrmions more efficiently.

Figure 9 shows the calculated phase diagram for the spin structures in a core-shell nanodisk with $R_{\text{core}} = 20\,\text{nm}$ and

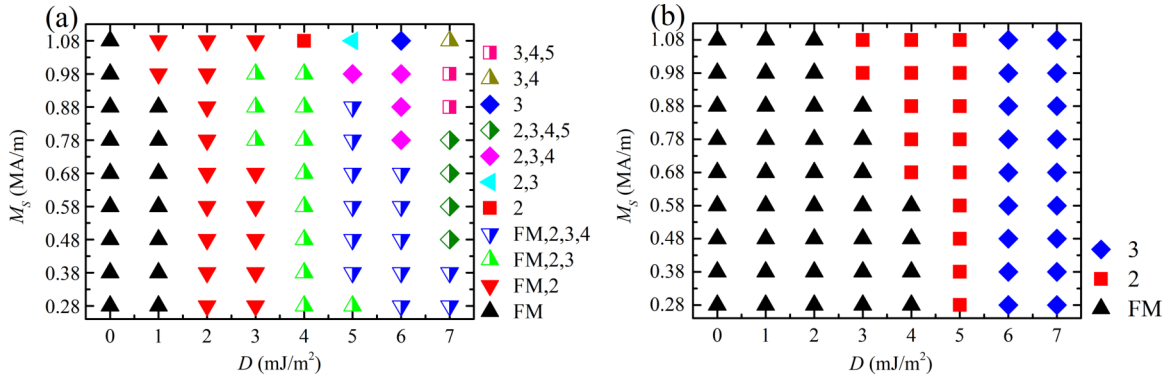

FIG. 7. Phase diagram for the spin structures in a single-phase CoPt nanodisk ($R = 40\,\text{nm}$) with various saturation magnetizations M_S and DMI constants D. (a) The M_S-D phase diagram of the possibly stable states, where the total energy is a local minimum. (b) The M_S-D phase diagram of the ground state. As the DMI increases, the ground state of the spin structures changes from the ferromagnetic (FM) state to the skyrmion and finally to the 2π-skyrmion. Here, 2–5 represent skyrmion states 1π–4π, respectively.

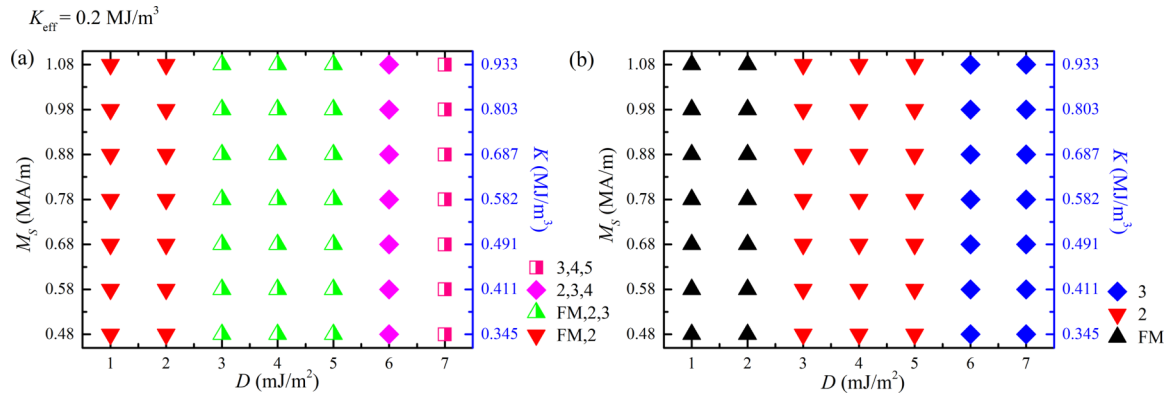

FIG. 8. Phase diagram for the spin structures in a core-shell structure disk ($R = 40$ nm) with various saturation magnetizations M_S, K and DMI constants D, where K_{eff} is fixed at 0.2 MJ/m^3. (a) The M_S, K-D phase diagram of the possibly stable states, where the total energy is a local minimum. (b) The M_S, K-D phase diagram of the ground state. As the DMI increases, the ground state of the spin structures changes from the ferromagnetic (FM) state to the skyrmion and finally to the 2π-skyrmion. Here, 2–4 represent skyrmion states 1π–3π, respectively.

$R = 40$ nm, where the inner core is CoPt, while the shell can be replaced with $Co_{20}Fe_{60}B_{20}$, which has a large M_S of 1100 kA/m [82]. Notably, the saturation magnetization M_S of a compound depends on the ratio of elements, and the CoPt adopted in this paper as an example normally appears in experiment as a multilayer or bilayer with Pt and Co arranged alternatively. Thus, the saturation magnetization M_S is controllable by altering the thickness of the heavy metal/magnetic metal or the percentage of the element occupation. The FM state can appear in such a core-shell disk only at relatively small DMI constants, as shown in Fig. 9(a) for the calculated possible states. When the shell DMI constant (D_{shell}) $\leqslant$ 3 mJ/m^2, various skyrmion states can exist along with the FM state, with the kinds of states increasing with the core DMI constant. However, when $D_{shell} \geqslant 4$ mJ/m^2, the FM state disappears so that skyrmion states might form spontaneously, no matter what the D_{core} is, where the skyrmion, 2π-skyrmion, and 3π-skyrmion might exist spontaneously. Particularly, it is noted that only the skyrmion can exist when $D_{shell} \geqslant 4$ mJ/m^2 and $D_{core} = 0$ mJ/m^2, shown in Fig. 9(a).

A similar change of the ground state with the DMI can be observed in Fig. 9(b), where the FM can be the ground state only when $D_{shell} \leqslant 4$ mJ/m^2. As the DMI increases, the ground state of the spin structures changes from the FM state to the skyrmion and finally to the 3π-skyrmion. In comparison, the spin structures are more sensitive to the DMI constant in the shell than that in the core. It can be seen from Fig. 9(b) that the skyrmion can be nucleated even if $D_{shell} = 4$ mJ/m^2 and $D_{core} = 0$ mJ/m^2, which can reduce the average DMI constant required for the skyrmion nucleation in comparison with the single-phase case, as shown in Fig. 4(b).

To gain deeper understanding of the phase-diagram, we have performed numerical calculations using the software package OOMMF including the extension module of the DMI and obtained various spin structures as ground states, shown in Fig. 10 for a core-shell nanodisk with $R = 40$ nm. The FM state remains for a small shell DMI constant (2 mJ/m^2), where the core DMI constant can vary from 2 to 5 mJ/m^2. As D_{shell} increases, the ground state changes from the FM state to the skyrmion and finally to the 2π-skyrmion. On the other hand, when $D_{shell} = 4$ mJ/m^2, the skyrmion state is kept as D_{core} increases from 2 to 6 mJ/m^2, with the center area of the skyrmion (marked by red in Fig. 10) contracting slightly. It is worth noting that the skyrmion can form spontaneously in a wide range of DMI constants; hence, it is convenient to create skyrmions freely in experiments

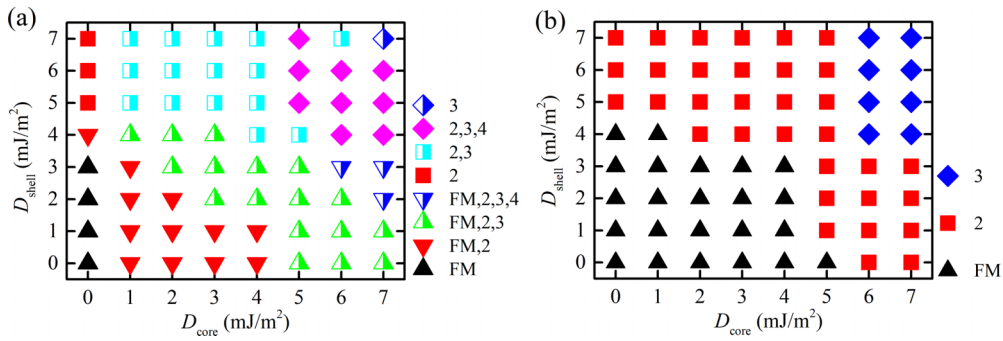

FIG. 9. Calculated phase diagram for the spin structures in a core-shell nanodisk with $R = 40$ nm and $R_{core} = 20$ nm, where the inner core is CoPt, while the shell has a large M_S of 1100 kA/m. (a) The D_{core}-D_{shell} phase diagram of the possibly stable states, where the total energy is a local minimum. (b) The D_{core}-D_{shell} phase diagram of the ground state. As the DMI increases, the ground state of the spin structures changes from the ferromagnetic (FM) state to the skyrmion and finally to the $k\pi$-skyrmion. Here, 2–4 represent the skyrmion states 1π–3π, respectively.

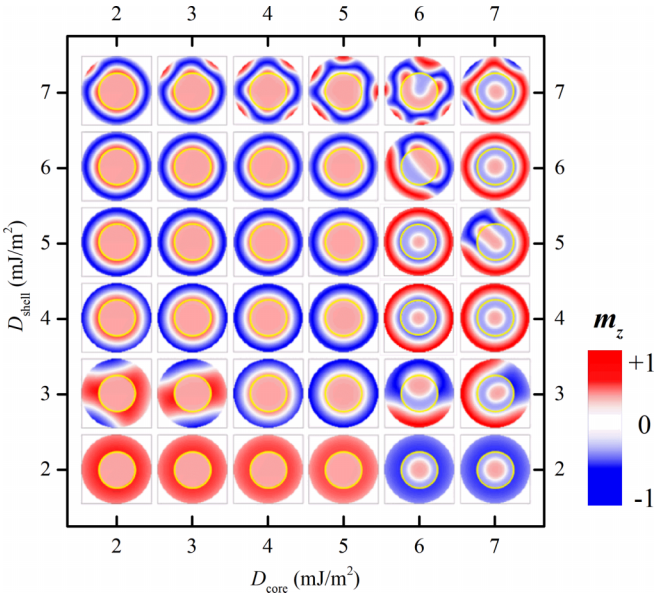

FIG. 10. Calculated spin structures formed spontaneously in a core-shell nanodisk with $R = 40$ nm and $R_{core} = 20$ nm by OOMMF, where the inner core is CoPt, while the shell has a large M_S of 1100 kA/m. In addition, the interface between the core and shell is represented by the solid yellow coil in the figure. The spin structures are obtained by relaxation for 4 ns starting from a ferromagnetic (FM) state, and 4 ns is fully sufficient for the system relaxation (see Appendix F). The color scale shows the out-of-plane component of magnetization m_z. In this calculation, strong interfacial exchange coupling $J = (A_{core} + A_{shell})/2a$ is adopted, where $a = 1$ nm is the length of the cell size.

with a similar nanodisk. Moreover, it should be noted that only circularly symmetric spin structures can be accounted in our analytical calculation. In contrast, the numerical calculation can include circularly unsymmetric spin structures (distorted structures). As demonstrated in Fig. 10, there are 12 distorted spin structures, which are close to the corresponding spin structures in Fig. 9(b). For example, when $D_{shell} = 3\,\mathrm{mJ/m^2}$, there are four distorted structures in Fig. 10, two for small D_{core} ($D_{core} = 2$ and $3\,\mathrm{mJ/m^2}$), and two for large D_{core} ($D_{core} = 6$ and $7\,\mathrm{mJ/m^2}$). The two distorted structures for small D_{core} are close to the FM state in Fig. 9(b), as one can see that most parts of these distorted structures are red (signifying the FM state) except a little blue. Similarly, the two distorted structures for large D_{core} are close to the skyrmion state in Fig. 9(b), especially for $D_{core} = 6\,\mathrm{mJ/m^2}$. A close examination of Fig. 10 for $D_{core} = 6\,\mathrm{mJ/m^2}$ (with $D_{shell} = 3\,\mathrm{mJ/m^2}$) shows that most of the shell is blue, whereas the core is in red, indicating a typical skyrmion state.

On the other hand, there are 24 circularly symmetric spin structures in Fig. 10, where only two are different from those shown in Fig. 9(b). When $D_{core} = 4\,\mathrm{mJ/m^2}$ and $D_{shell} = 3\,\mathrm{mJ/m^2}$, a skyrmion is formed as a ground state rather than a FM state in Fig. 9(b). When $D_{core} = 5\,\mathrm{mJ/m^2}$ and $D_{shell} = 2\,\mathrm{mJ/m^2}$, a FM state is formed as a ground state in Fig. 10, whereas a skyrmion state appears in Fig. 9(b). These differences are mainly due to the calculational error arising from the numerical calculation. It is noted that the cell size in our simulation is adopted as 1 nm due to the restrict of the computational sources, which might cause some errors. Further study shows that the phase boundary between the skyrmion state and the FM state in the simulation is about $D_{core} = 5.1\,\mathrm{mJ/m^2}$ (with $D_{shell} = 2\,\mathrm{mJ/m^2}$).

We also carefully compared the energy of the ground state in the core-shell nanodisk with $D_{shell} = 5\,\mathrm{mJ/m^2}$ based on both numerical and variational methods, as shown in Fig. 11(a). One can see that the total energies of the spin states calculated based on our analytical and numerical method agree very well, especially for small DMI constants ($D_{core} \leqslant 3\,\mathrm{mJ/m^2}$), where the relative error is <3%. When the DMI constant is large, the total energy calculated based on the numerical method deviates more from those by the analytical method, where the error can exceed 8%. Additionally, we make a comparison for the magnetostatic energy of different spin structures calculated based on the two methods, which are shown in Fig. 11(b). One can see that the energy difference here is <9%, where the largest difference occurs at large DMIs. For small DMIs, the energy difference is much smaller. For example, when $D_{core} = 3\,\mathrm{mJ/m^2}$ and $D_{shell} = 5\,\mathrm{mJ/m^2}$,

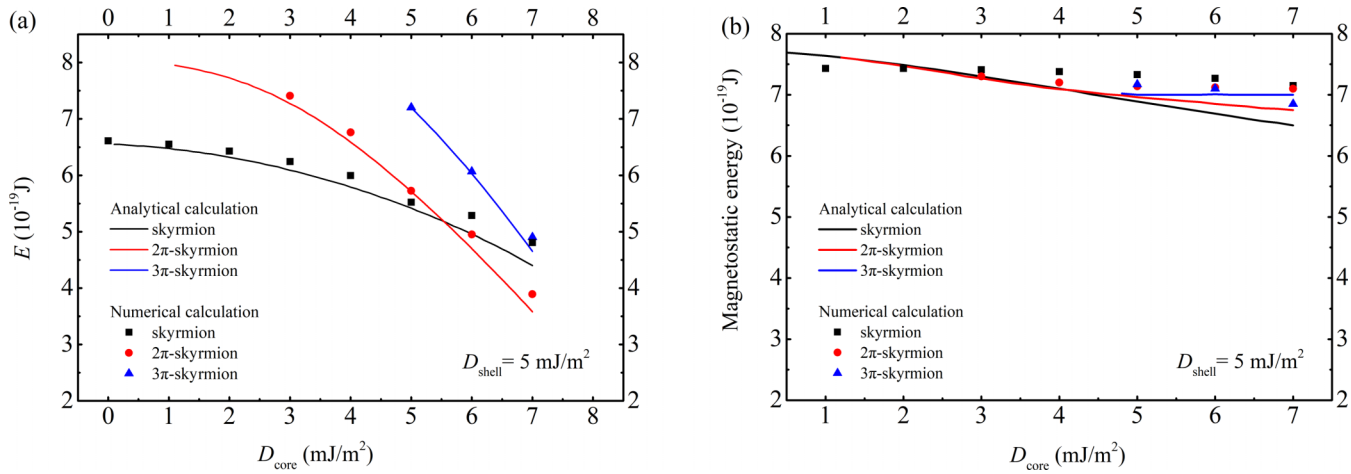

FIG. 11. Comparison of the (a) total energy E and (b) the magnetostatic energy calculated by the analytical and numerical methods for different spin structures in a core-shell nanodisk with $R = 40$ nm and $R_{core} = 20$ nm, where $D_{shell} = 5\,\mathrm{mJ/m^2}$.

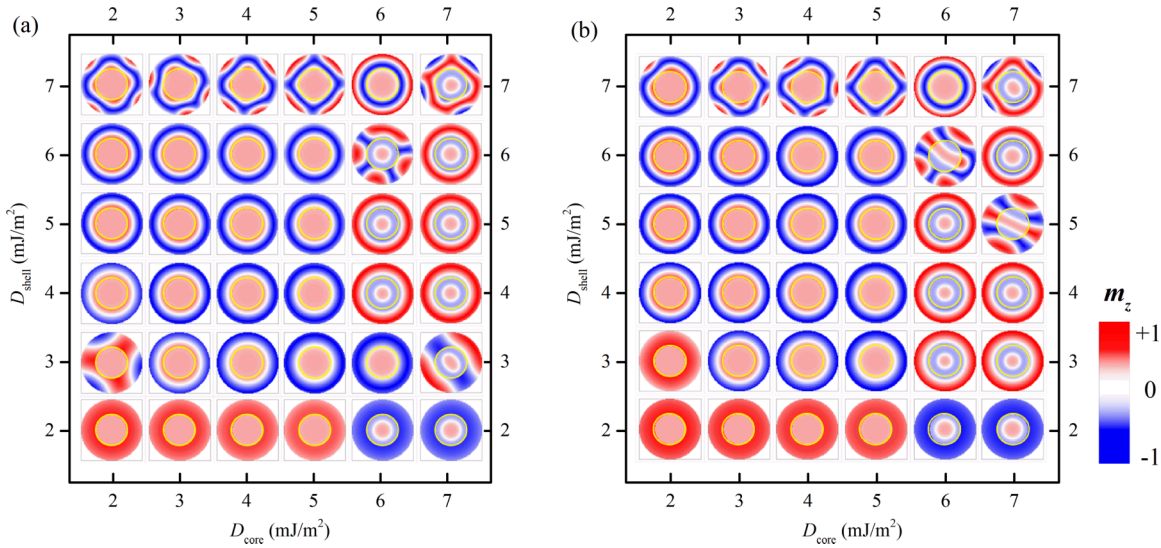

FIG. 12. Calculated spin structures formed spontaneously in a core-shell nanodisk with $R = 40$ nm and $R_{core} = 20$ nm by OOMMF, where the inner core is CoPt, while the shell has a large M_S of 1100 kA/m. (a) The D_{core}-D_{shell} phase diagram of the ground state, where the exchange constant at the core-shell interface $J = (A_{core} + A_{shell})/4a$ and $h = 0.4$ nm. (b) The D_{core}-D_{shell} phase diagram of the ground state, where the thickness of the nanodisk $h = 0.8$ nm and $J = (A_{core} + A_{shell})/2a$. In addition, the interface between the core and shell is represented by the solid yellow circle in the figure. The spin structures are obtained by relaxation for 4 ns starting from a ferromagnetic (FM) state. The color scale shows the out-of-plane component of magnetization m_z.

the magnetostatic energy calculated based on the micromagnetic simulation for a skyrmion is 7.4109×10^{-19} J, while the magnetostatic energy calculated based on the analytical method is 7.3096×10^{-19} J. Here, the energy difference is only ~1.36%.

It is noteworthy that the spin structures formed spontaneously in a core-shell nanodisk are not sensitive to the interfacial coupling strength of the core-shell nanodisk, as shown in Fig. 12(a). On the other hand, we find that the spin states in the core-shell nanodisk with $h = 0.8$ nm [Fig. 12(b)] are like those with $h = 0.4$ nm (Fig. 10), indicating that the spin structures are not sensitive to the thickness of the core-shell nanodisk (see Appendix G). Moreover, our present result can be obtained with the smooth variation of the DMI constant D and saturation magnetization Ms at the interface, as shown in Fig. 13. See Appendix H for more details.

More complex skyrmion configurations can be nucleated if a spin current is applied in the abovementioned core-shell nanodisk. We have calculated spin structures generated in a core-shell nanodisk with $R = 75$ nm and $R_{core} = 40$ nm using OOMMF, by injecting the spin-polarized current perpendicularly with the density of 5×10^{12} A/m^2 in the central circle with a radius of 20 nm for various DMI constants D. It can be seen from Fig. 14, as the DMI constant increases, the spin structure tends to become $k\pi$-skyrmion, and the number of domains becomes more and more. For example, the skyrmion state cannot be found when the DMI constant of the nanodisk is 1 mJ/m^2 so that only the FM state can exist. As the DMI constant increases, the skyrmion and 2π-skyrmion are nucleated when the DMI constants are 2 and 3 mJ/m^2, respectively. Further increase of the DMI constant to 4 or 5 mJ/m^2 will lead to the 4π-skyrmion. The 4π-skyrmion structure remains until $D_{core} = D_{shell} = 8$ mJ/m^2, when the 5π-skyrmion forms instead.

It should be noted that, before the Néel-type skyrmions form, as shown in Fig. 14, they first occur in the form of Bloch-type skyrmions, as shown in Fig. 15, possibly owing to the small energy barrier between the vortex state and the FM state. The Bloch-type skyrmions then evolve to Néel-type skyrmions because the DMI here favors Néel-type skyrmions rather than the Bloch ones. These stable states are included in

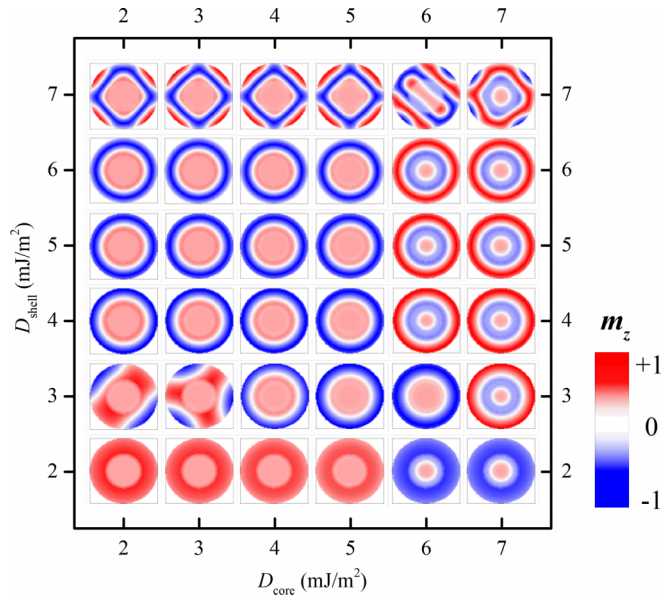

FIG. 13. Calculated spin structures formed spontaneously in a core-shell nanodisk with $R = 40$ nm, $R_{core} = 18$ nm, and $R_{interface} = 4$ nm by OOMMF, where the inner core is CoPt, while the shell has a large M_S of 1100 kA/m. In this calculation, the smooth variation of D and M_S at the interface is adopted.

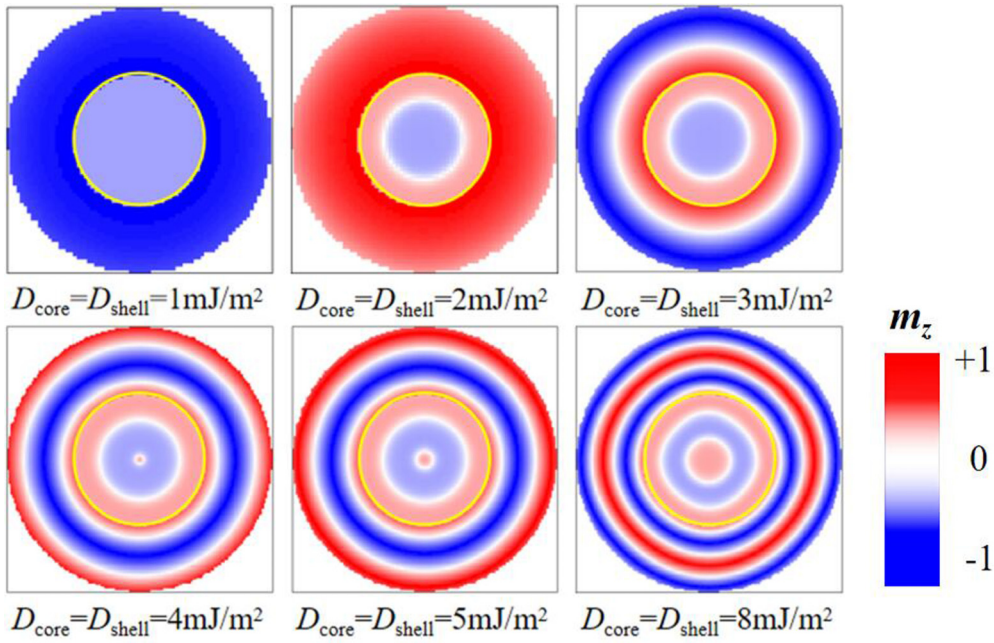

FIG. 14. Calculated spin structures generated in a core-shell nanodisk with $R = 75$ nm and $R_{core} = 37.5$ nm using OOMMF, by injecting the spin-polarized current perpendicularly. The solid yellow line indicates the interface between the core and shell.

Fig. 9(a) which, however, are not necessarily the ground state displayed in Fig. 9(b) (see Appendix E).

We have also nucleated various Néel-type skyrmions using OOMMF software in a single-phase CoPt disk with $R = 40$ nm by injecting a spin current of 5×10^{12} A/m^2, as shown in Fig. 16(a). To justify our calculation, we make a careful comparison for the total energies calculated based on the two methods, as shown in Fig. 16(b). One can see that our analytical and numerical calculations agree very well with each other, especially for small DMI constants ($D \leqslant 4$ mJ/m^2), where the relative error is <2.5%. Our analytically calculated energies also match well with the numerical results of Sampaio *et al.* [16], with the error <2% for small D. For large D, the error becomes larger, which can exceed 10%. The match of the numerical results by the two groups is better, where the error is <4% for all values of DMI constants. Our analyses show that the relative error can be much reduced if the mesh size in the numerical calculation is decreased.

IV. CONCLUSIONS

In summary, we have proposed a variational method which can predict the rich topological states in both single-phased and core-shell nanodisks efficiently, with the validity confirmed by carefully comparing with available experimental and numerical results. This method is basically an analytical one, which has been used in this paper to search for various skyrmion states along with the commonly used numerical methods. These skyrmion states can be used in the future as various kinds of storage units, enriching the related topological physics as well as applications beyond. It is found that various skyrmion states can form spontaneously in a

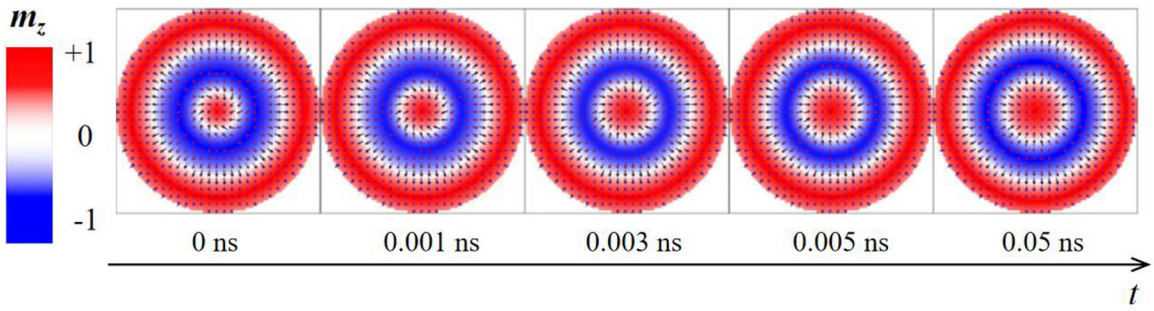

FIG. 15. Evolution of a Néel-like skyrmion from a spin structure with a Bloch-like core and a Néel-like shell in a core-shell structure disk ($R_{core} = 40$ nm) with $D = 6$ mJ/m^2, which displays the relaxation of the spin structure in the disk in zero field generated by application of a spin current with density of 5×10^{12} A/m^2 for 2 ns in the 40-nm inner disk.

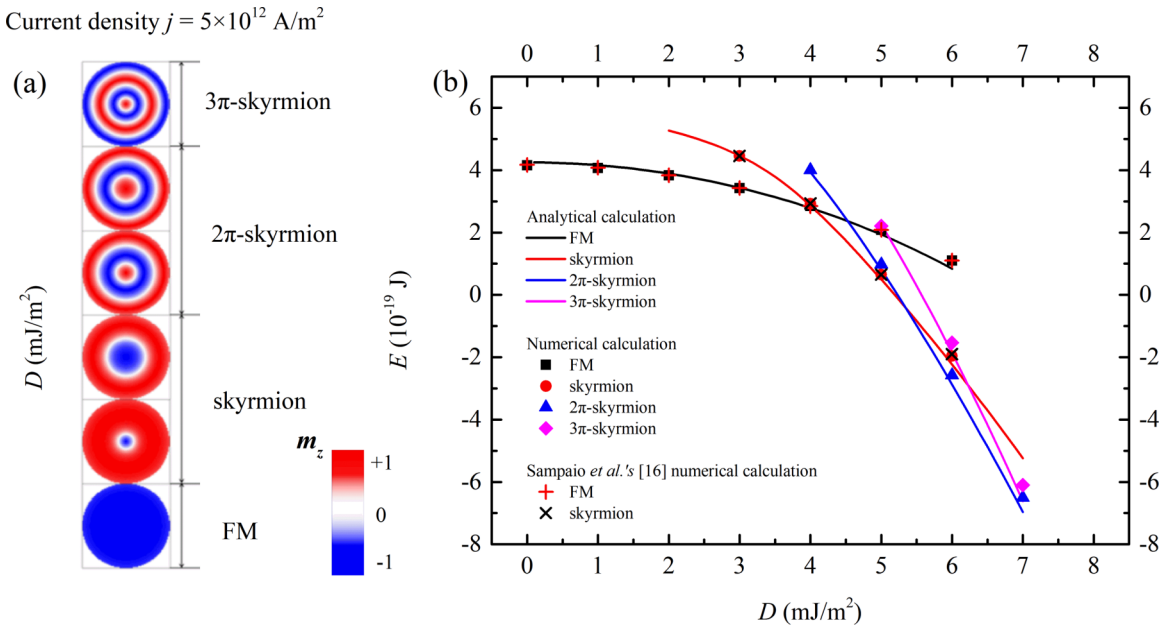

FIG. 16. (a) Spin structures generated in a single-phase CoPt nanodisk by injecting the spin-polarized current with the density of 5×10^{12} A/m^2 for various DMI constants D. As the DMI increases, the generated spin structures change from the ferromagnetic (FM) state to the skyrmion, then to the 2π-skyrmion, and finally to the 3π-skyrmion. (b) Comparison of the total energy E calculated by the analytical and numerical methods for different spin structures; the numerical results by Sampaio *et al.* [16] are also shown for comparison.

core-shell nanodisk with much smaller DMIs in comparison with traditional methods, which facilitates the realization of skyrmions significantly.

ACKNOWLEDGMENTS

G.Z. acknowledges the support by the National Natural Science Foundation of China (Grants No. 51771127, No. 52171188, and No. 52111530143) of China, and the Central Government Funds of Guiding Local Scientific and Technological Development for Sichuan Province (No. 2021ZYD0025). J.X. acknowledges the support from the National Natural Science Foundation of China (Grant No. 12104327). Y.Z. acknowledges the support from Guangdong Basic and Applied Basic Research Foundation (No. 2021B1515120047), Guangdong Special Support Project (No. 2019BT02 × 030), Shenzhen Fundamental Research Fund (Grant No. JCYJ20210324120213037), Shenzhen Peacock Group Plan (No. KQTD20180413181702403), Pearl River Recruitment Program of Talents (No. 2017GC010293), and National Natural Science Foundation of China (No. 11974298 and No. 61961136006).

S.L. and Q.L. contributed equally to this paper.

APPENDIX A: THE MAGNETOSTATIC INTERACTIONS BETWEEN THE CORE AND SHELL REGIONS

The magnetostatic interactions between the core and shell regions are not included in the total energy in our analytical calculation (which, however, has been included in the numerical calculation) because it is not important. To justify this, we make a comparison for the total magnetostatic energy of different spin structures calculated based on the two methods, which are roughly consistent with each other, as shown in Fig. 11(b).

To further justify the issue, we have calculated the total magnetostatic energy in uniformly magnetized (in the z direction) core-shell nanodisks by micromagnetic simulation, which is 1.2213×10^{-18} J. In this case, the magnetostatic energy can also be calculated analytically, where the dipolar coupling can be assumed by the shape anisotropy in the zero-thickness limit [83]. The magnetostatic field can be approximated as $N\mathbf{M}$ with $N_z = 1$. Noting that the magnetostatic interactions obey the superposition principle [84], the magnetization $\mathbf{M}$ of the core-shell nanodisk can be divided into $\mathbf{M}_1$ of the whole nanodisk with $M_S = M_{\text{shell}}$ and $\mathbf{M}_2$ of the core region with $M_S = M_{\text{core}} - M_{\text{shell}}$, where the orientation of magnetic moments is the same for $\mathbf{M}$, $\mathbf{M}_1$, and $\mathbf{M}_2$. Thus, the total magnetostatic field for a core-shell nanodisk can be approximated as

$$\begin{aligned}\boldsymbol{H}_{\text{D}}(\mathbf{M}) &= N_{\text{whole}}\mathbf{M}_1 + N_{\text{core}}\mathbf{M}_2 \\ &= \begin{cases} M_{\text{core}}\cos\theta, & r \in [0, R_{\text{core}}), \\ M_{\text{shell}}\cos\theta, & r \in (R_{\text{core}}, R], \end{cases}\end{aligned} \tag{A1}$$

where N_{whole} and N_{core} are the demagnetizing factor ($\sim$1) for the whole nanodisk and the core part, while M_{core} and M_{shell} represent the saturation magnetization of the nanodisk in the core and shell, and H_{D} represents the total demagnetizing field.

Therefore, in the core-shell nanodisk, the total magnetostatic energy can be expressed as

$$\begin{aligned}E_{\text{demag}} &= 2\pi h \int_0^{R_{\text{core}}} \frac{1}{2}\mu_0 M_{\text{core}}^2 \cos^2\theta r dr \\ &\quad + 2\pi h \int_{R_{\text{core}}}^{R} \frac{1}{2}\mu_0 M_{\text{shell}}^2 \cos^2\theta r dr.\end{aligned} \tag{A2}$$

The total magnetostatic energy for the core-shell nanodisk is the same as Eq. (11). Please note that the magnetostatic interactions between the core and shell regions have been included in this derivation process, i.e., in Eq. (A1), whereas it is ignored in Eq. (11), indicating that the magnetostatic interactions between the core and shell regions can be neglected. By the way, the total magnetostatic energy for a uniformly magnetized core-shell nanodisk in the z direction calculated by Eq. (11) is 1.2528×10^{-18} J with an error of $<2.5\%$ in comparison with that based on the micromagnetic simulation. This error, however, is largely because, in the analytical method, the demagnetizing factors in the nanodisk are 0.969 (core) and 0.982 (core-shell) rather than ~ 1 [85], indicating that our approximation is valid.

APPENDIX B: PHASE DIAGRAM FOR THE SPIN STRUCTURES WITH VARIOUS EXCHANGE CONSTANTS A AND DMI CONSTANTS D

The possible energy-minimized spin states and the ground state of the FM nanodisks are not only affected by the DMI constant and the nanodisk size but also change with other material parameters. The exchange stiffness A has a significant influence on the spin states, especially when the DMI constant is large, as shown in Fig. 5, where the angle of rotation in the direction of magnetization is more (such as 5π- and 6π-skyrmions) for smaller values of A. On the other hand, the influence of the DMI in both (a) and (b) is like Fig. 4, where the angle of rotation in the direction of magnetization is more (such as 5π- and 6π-skyrmions) for larger values of D.

Moreover, the ground state (i.e., the state with the lowest energy) shown in Fig. 5(b) varies with A and D. The FM state is the most stable state for $D < 3\,\mathrm{mJ/m^2}$, as A varies in the range of 8–20 pJ/m. However, the ground state transforms from the FM state to the skyrmion state with increasing D. Moreover, the $k\pi$-skyrmion state is more likely to occur as D increases and A decreases.

APPENDIX C: PHASE DIAGRAM FOR THE SPIN STRUCTURES WITH VARIOUS CRYSTALLINE ANISOTROPY CONSTANTS K AND DMI CONSTANTS D

One can see the phase diagram of the possible energy-minimized states and the ground state for different crystalline anisotropy constants K and DMI constants D from Fig. 6. In Fig. 6(a), similarly, the smaller the value of K, the higher the probability for $k\pi$-skyrmion states. The FM state disappears only in a small range of K and D. It should be noted that the phase diagram of the ground state is mostly occupied by the FM state, and the 2π-skyrmion is the ground state with the most angles of rotation in the direction of magnetization.

APPENDIX D: PHASE DIAGRAM FOR THE SPIN STRUCTURES WITH VARIOUS SATURATION MAGNETIZATIONS M_S AND DMI CONSTANTS D

Figure 7 shows the phase diagram of the possible energy-minimized states and the ground state for different saturation magnetizations Ms and DMI constants D. As shown in Fig. 7, the spin states are not sensitive to the value of M_S when D is small, especially for the ground state in Fig. 7(b). When the DMI constant is large, M_S has a relatively larger effect on the spin state, where the larger the value of M_S, the higher the probability for higher-order skyrmion states.

Further, we discussed the spin structures with various values of M_S and DMI constants D in Fig. 8 , where K_{eff} is fixed at $0.2\,\mathrm{MJ/m^3}$. From Fig. 8, we can see that the spin structures are the same for fixed K_{eff} with various values of M_S, indicating that the spin structures are affected by the saturation magnetization M_S mainly through the effective magnetic anisotropy K_{eff} ($K_{\mathrm{eff}} = K - \frac{1}{2}\mu_0 M_s^2$).

APPENDIX E: EVOLUTION OF A NÉEL-LIKE SKYRMION

We first nucleate a 2π-skyrmion in a nanodisk ($R = 40\,\mathrm{nm}$) when $D = 6\,\mathrm{mJ/m^2}$ by injecting a 2-ns-long spin-polarized current with density of $5 \times 10^{12}\,\mathrm{A/m^2}$ and then relax it in zero field for 2 ns. Figure 15 illustrates the process of the relaxation, and at $t = 0$ ns, the 2π-skyrmion is Bloch-like, and then the vorticity of the magnetizations reduces gradually with time. Finally, the Bloch-like skyrmion turns into a Néel-like skyrmion at $t = 0.05$ ns. Moreover, the 2π-skyrmion expands with time and ultimately reaches a stable state within the relaxation time.

APPENDIX F: EVOLUTION OF A NÉEL-SKYRMIONIUM

We construct a FM state as the initial state and then relax it in zero field for 20 ns. Figure 17 illustrates the process of the relaxation, and at $t = 0.1$ ns, the skyrmion is Néel-like. Then the magnetizations of the shell evolve gradually with time, and a skyrmionium is formed and stabilized when $t = 0.3$ ns. This skyrmionium state is retained until $t = 20$ ns, demonstrating that 4 ns is sufficient for the relaxation of the system.

APPENDIX G: SPIN STRUCTURES FORMED SPONTANEOUSLY IN A CORE-SHELL NANODISK WITH $J = \frac{1}{4a}(A_{\mathrm{core}} + A_{\mathrm{shell}})$ AND $h = 0.8\,\mathrm{nm}$

In Fig. 12(a), we find that the spin states in a core-shell nanodisk with weak coupling $J = (A_{\mathrm{core}} + A_{\mathrm{shell}})/4a$ are like those with strong coupling $J = (A_{\mathrm{core}} + A_{\mathrm{shell}})/2a$ (Fig. 10), indicating that the spin structures are not sensitive to the interfacial coupling strength of the core-shell nanodisk. Interestingly, compared with the case with strong coupling, there are more skyrmion states in Fig. 12(a), which suggests that the skyrmion is more likely to appear in the core-shell nanodisk with weak coupling. In Fig. 12(b), we find that the spin states in a core-shell nanodisk with $h = 0.8$ nm are like those with $h = 0.4$ nm (Fig. 10), indicating that the spin structures are not sensitive to the thickness of the core-shell nanodisk. Interestingly, when $D_{\mathrm{core}} = 6\,\mathrm{mJ/m^2}$, $D_{\mathrm{shell}} = 3,\ 6\,\mathrm{mJ/m^2}$ and $D_{\mathrm{core}} = 7\,\mathrm{mJ/m^2}$, $D_{\mathrm{shell}} = 3\,\mathrm{mJ/m^2}$, a 2π-skyrmion can be formed as a ground state in Fig. 12(b) rather than a distorted spin structure formed in Fig. 10, suggesting that the skyrmion is more likely to appear in the core-shelled nanodisk with large thickness.

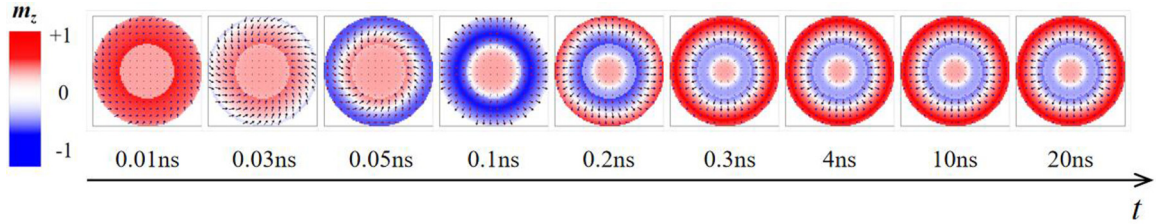

FIG. 17. Evolution of a Néel-skyrmionium from a ferromagnetic (FM) state in a core-shell structure disk with $R = 40\,\text{nm}$ and $R_{\text{core}} = 20\,\text{nm}$, where $D_{\text{core}} = 7\,\text{mJ/m}^2$, $D_{\text{shell}} = 4\,\text{mJ/m}^2$, which displays the relaxation of the spin structure in the disk in zero field.

APPENDIX H: CALCULATED SPIN STRUCTURES FORMED SPONTANEOUSLY IN A CORE-SHELL NANODISK WITH THE SMOOTH VARIATION OF D AND M_S AT THE INTERFACE

Figure 13 shows the ground states of the core-shell nanodisk with the smooth variation of D and Ms at the interface. We find that all of the skyrmion states in Fig. 10 are like our current numerical results, demonstrating that similar results could be obtained with the smooth variation of D and M_S at the interface. Further, it is noted that the spin structures are more regular for the smooth variation of the parameters. For example, when $D_{\text{core}} = 6\,\text{mJ/m}^2$ and $D_{\text{shell}} = 3\,\text{mJ/m}^2$, a symmetric skyrmion state rather than a distorted spin structure occurs as a ground state in Fig. 13. Similarly, when $D_{\text{core}} = 7\,\text{mJ/m}^2$ and $D_{\text{shell}} = 6\,\text{mJ/m}^2$, a skyrmionium state appears as a ground state in Fig. 13 for the smooth variation of the parameters, whereas a distorted spin structure is shown in Fig. 10 for an abrupt change of parameters.

[1] T. H. R. Skyrme, Nucl. Phys. **31**, 556 (1962).
[2] S. L. Sondhi, A. Karlhede, S. A. Kivelson, and E. H. Rezayi, Phys. Rev. B **47**, 16419 (1993).
[3] T. Sakai and S. Sugimoto, Prog. Theor. Phys. **113**, 843 (2005).
[4] U. K. Rößler, A. N. Bogdanov, and C. Pfleiderer, Nature (London) **442**, 797 (2006).
[5] N. Nagaosa and Y. Tokura, Nat. Nanotechnol. **8**, 899 (2013).
[6] W. Kang, Y. Q. Huang, X. C. Zhang, Y. Zhou, and W. S. Zhao, Proc. IEEE **104**, 2040 (2016).
[7] G. Finocchio, F. Büttner, R. Tomasello, M. Carpentieri, and M. Kläui, J. Phys. D: Appl. Phys. **49**, 423001 (2016).
[8] W. J. Jiang, G. Chen, K. Liu, J. D. Zang, S. G. E. te Velthuis, and A. Hoffmann, Phys. Rep. **704**, 1 (2017).
[9] A. Fert, N. Reyren, and V. Cros, Nat. Rev. Mater. **2**, 17031 (2017).
[10] N. Kanazawa, S. Seki, and Y. Tokura, Adv. Mater. **29**, 1603227 (2017).
[11] K. Everschor-Sitte, J. Masell, R. M. Reeve, and M. Kläui, J. Appl. Phys. **124**, 240901 (2018).
[12] X. Liang, L. Zhao, L. Qiu, S. Li, L. H. Ding, Y. H. Feng, X. C. Zhang, Y. Zhou, and G. P. Zhao, Acta Phys. Sin. **67**, 137510 (2018).
[13] Y. Zhou, Natl. Sci. Rev. **6**, 210 (2019).
[14] X. C. Zhang, Y. Zhou, K. M. Song, T. Park, J. Xia, M. Ezawa, X. X. Liu, W. S. Zhao, G. P. Zhao, and S. Woo, J. Phys.: Condens. Matter **32**, 143001 (2020).
[15] C. Ye, L. L. Li, Y. Shu, Q. R. Li, J. Xia, Z. P. Hou, Y. Zhou, X. X. Liu, Y. Y. Yang, and G. P. Zhao, Rare Met. **41**, 2200 (2022).
[16] J. Sampaio, V. Cros, S. Rohart, A. Thiaville, and A. Fert, Nat. Nanotechnol. **8**, 839 (2013).
[17] A. Fert, V. Cros, and J. Sampaio, Nat. Nanotechnol. **8**, 152 (2013).
[18] R. Tomasello, E. Martinez, R. Zivieri, L. Torres, M. Carpentieri, and G. Finocchio, Sci. Rep. **4**, 6784 (2014).
[19] L. C. Shen, J. Xia, X. C. Zhang, M. Ezawa, O. A. Tretiakov, X. X. Liu, G. P. Zhao, and Y. Zhou, Phys. Rev. Lett. **124**, 037202 (2020).
[20] X. C. Zhang, G. P. Zhao, H. Fangohr, J. P. Liu, W. X. Xia, J. Xia, and F. J. Morvan, Sci. Rep. **5**, 7643 (2014).
[21] W. Koshibae, Y. Kaneko, J. Iwasaki, M. Kawasaki, Y. Tokura, and N. Nagaosa, Jpn. J. Appl. Phys. **54**, 053001 (2015).
[22] P. Lai, G. P. Zhao, H. Tang, N. Ran, S. Q. Wu, J. Xia, X. C. Zhang, and Y. Zhou, Sci. Rep. **7**, 45330 (2017).
[23] P. Lai, G. P. Zhao, F. J. Morvan, S. Q. Wu, and N. Ran, Spin **7**, 1740006 (2017).
[24] X. C. Zhang, M. Ezawa, and Y. Zhou, Sci. Rep. **5**, 9400 (2015).
[25] X. J. Xing, P. W. T. Pong, and Y. Zhou, Phys. Rev. B **94**, 054408 (2016).
[26] S. J. Luo, M. Song, X. Li, Y. Zhang, J. Hong, X. F. Yang, X. C. Zou, N. Xu, and L. You, Nano Lett. **18**, 1180 (2018).
[27] X. Liang, J. Xia, X. C. Zhang, M. Ezawa, O. A. Tretiakov, X. X. Liu, L. Qiu, G. P. Zhao, and Y. Zhou, Appl. Phys. Lett. **119**, 062403 (2021).
[28] X. C. Zhang, Y. Zhou, M. Ezawa, G. P. Zhao, and W. S. Zhao, Sci. Rep. **5**, 11369 (2015).
[29] J. Xia, Y. Q. Huang, X. C. Zhang, W. Kang, C. T. Zheng, X. X. Liu, W. S. Zhao, and Y. Zhou, J. Appl. Phys. **122**, 153901 (2017).
[30] L. Zhao, X. Liang, J. Xia, G. P. Zhao, and Y. Zhou, Nanoscale **12**, 9507 (2020).
[31] L. C. Shen, J. Xia, G. P. Zhao, X. C. Zhang, M. Ezawa, O. A. Tretiakov, X. X. Liu, and Y. Zhou, Appl. Phys. Lett. **114**, 042402 (2019).
[32] Y. H. Feng, J. Xia, L. Qiu, X. R. Cai, L. C. Shen, F. J. Morvan, X. C. Zhang, Y. Zhou, and G. P. Zhao, J. Magn. Magn. Mater. **491**, 165610 (2019).
[33] X. Liang, X. C. Zhang, J. Xia, M. Ezawa, Y. L. Zhao, G. P. Zhao, and Y. Zhou, Appl. Phys. Lett. **116**, 122402 (2020).

[34] K. M. Song, J. S. Jeong, B. Pan, X. C. Zhang, J. Xia, S. Cha, T. E. Park, K. Kim, S. Finizio, J. Raabe *et al.*, Nat. Electron. **3**, 148 (2020).

[35] S. Mühlbauer, B. Binz, F. Jonietz, C. Pfleiderer, A. Rosch, A. Neubauer, R. Georgii, and P. Böni, Science **323**, 915 (2009).

[36] C. Pfleidere and A. Rosch, Nature (London) **465**, 880 (2010).

[37] X. Z. Yu, N. Kanazawa, Y. Onose, K. Kimoto, W. Z. Zhang, S. Ishiwata, Y. Matsui, and Y. Tokura, Nat. Mater. **10**, 106 (2011).

[38] S. X. Huang and C. L. Chien, Phys. Rev. Lett. **108**, 267201 (2012).

[39] S. Sek, X. Z. Yu, S. Ishiwata, and Y. Tokura, Science **336**, 198 (2012).

[40] T. Adams, A. Chacon, M. Wagner, A. Bauer, G. Brandl, B. Pedersen, H. Berge, P. Lemmens, and C. Pfleiderer, Phys. Rev. Lett. **108**, 237204 (2012).

[41] X. Z. Yu, Y. Onose, N. Kanazawa, J. Park, J. H. Han, Y. Matsui, N. Nagaosa, and Y. Tokura, Nature (London) **465**, 901 (2010).

[42] Y. Xiao, F. J. Morvan, A. N. He, M. K. Wang, H. B. Luo, R. B. Jiao, W. X. Xia, G. P. Zhao, and J. P. Liu, Appl. Phys. Lett. **117**, 132402 (2020).

[43] J. Barker and O. A. Tretiakov, Phys. Rev. Lett. **116**, 147203 (2016).

[44] L. C. Shen, J. Xia, G. P. Zhao, X. C. Zhang, M. Ezawa, O. A. Tretiakov, X. X. Liu, and Y. Zhou, Phys. Rev. B **98**, 134448 (2018).

[45] X. Liang, G. P. Zhao, L. C. Shen, J. Xia, L. Zhao, X. C. Zhang, and Y. Zhou, Phys. Rev. B **100**, 144439 (2019).

[46] J. Y. Zhang, Y. Zhang, Y. Gao, G. P. Zhao, L. Qiu, K. Y. Wang, P. W. Dou, W. L. Peng, Y. Zhuang, Y. F. Wu *et al.*, Adv. Mater. **32**, 1907452 (2020).

[47] A. K. Nayak, V. Kumar, T. Ma, P. Werner, E. Pippel, R. Sahoo, F. Damay, U. K. Rößler, C. Felser, and S. S. P. Parkin, Nature (London) **548**, 561 (2017).

[48] L. Qiu, J. Xia, Y. H. Feng, L. C. Shen, F. J. Morvan, X. C. Zhang, X. X. Liu, L. H. Xie, Y. Zhou, and G. P. Zhao, J. Magn. Magn. Mater. **496**, 165922 (2020).

[49] X. Z. Yu, Y. Tokunaga, Y. Kaneko, W. Z. Zhang, K. Kimoto, Y. Matsui, Y. Taguchi, and Y. Tokura, Nat. Commun. **5**, 3198 (2014).

[50] X. F. Xiao, L. C. Peng, X. G. Zhao, Y. Zhang, Y. Y. Dai, J. Guo, M. Tong, J. Li, B. Li, W. Liu *et al.*, Appl. Phys. Lett. **114**, 142404 (2019).

[51] A. Bogdanov and A. Hubert, J. Magn. Magn. Mater. **195**, 182 (1999).

[52] M. Finazzi, M. Savoini, A. R. Khorsand, A. Tsukamoto, A. Itoh, L. Duò, A. Kirilyuk, T. Rasing, and M. Ezawa, Phys. Rev. Lett. **110**, 177205 (2013).

[53] S. Komineas and N. Papanicolaou, Phys. Rev. B **92**, 064412 (2015).

[54] S. L. Zhang, A. Bauer, D. M. Burn, P. Milde, E. Neuber, L. M. Eng, H. Berger, C. Pfleiderer, G. van der Laan, and T. Hesjedal, Nano Lett. **16**, 3285 (2016).

[55] H. Fujita and M. Sato, Phys. Rev. B **95**, 054421 (2017).

[56] X. Y. Liu, Q. Y. Zhu, S. F. Zhang, Q. F. Liu, and J. B. Wang, AIP Advances **5**, 087137 (2015).

[57] X. C. Zhang, J. Xia, Y. Zhou, D. W. Wang, X. X. Liu, W. S. Zhao, and M. Ezawa, Phys. Rev. B **94**, 094420 (2016).

[58] M. K. Shen, Y. Zhang, J. Ou-Yang, X. F. Yang, and L. You, Appl. Phys. Lett. **112**, 062403 (2018).

[59] S. D. Pollard, J. A. Garlow, J. Yu, Z. Wang, Y. Zhu, and H. Yang, Nat. Commun. **8**, 14761 (2017).

[60] S. Woo, K. Litzius, B. Krüger, M. Y. Im, L. Caretta, K. Richter, M. Mann, A. Krone, R. M. Reeve, M. Weigand *et al.*, Nat. Mater. **15**, 501 (2016).

[61] O. Boulle, J. Vogel, H. X. Yang, S. Pizzini, D. Souza Chaves, A. Locatelli, T. O. Mentes, A. Sala, L. D. Buda-Prejbeanu, O. Klein *et al.*, Nat. Nanotechnol. **11**, 449 (2016).

[62] J. Xia, X. Zhang, F. J. Morvan, G. P. Zhao, and Y. Zhou, IEEE Trans. Magn. **51**, 1500303 (2015).

[63] W. Wang and A. Du, J. Magn. Magn. Mater **511**, 166591 (2020).

[64] A. López-Ortega, M. Estrade, G. Salazar-Alvarez, A. G. Roca, and J. Nogués, Phys. Rep. **553**, 1 (2014).

[65] W. Brown, *Micromagnetics* (Wiley, New York, 1963).

[66] A. Hubert and R. Schäfer, *Magnetic Domains* (Springer, Berlin, 1998).

[67] S. Rohart and A. Thiaville, Phys. Rev. B **88**, 184422 (2013).

[68] M. J. Donahue and D. G. Porter, OOMMF user's guide, Version 1.0 (1999).

[69] O. Boulle, L. D. Buda-Prejbeanu, E. Jué, I. M. Miron, and G. Gaudin, J. Appl. Phys. **115**, 17D502 (2014).

[70] T. L. Gilbert, Phys. Rev. **100**, 1243 (1955).

[71] L. Landau and E. Lifshitz, Phys. Z. Sowjetunion **8**, 153 (1935).

[72] W. Kang, Y. Q. Huang, C. T. Zheng, W. F. Lv, N. Lei, Y. G. Zhang, X. C. Zhang, Y. Zhou, and W. S. Zhao, Sci. Rep. **6**, 23164 (2016).

[73] N. Romming, C. Hanneken, M. Menzel, J. E. Bickel, B. Wolter, K. Bergmann, A. Kubetzka, and R. Wiesendanger, Science **341**, 636 (2013).

[74] P. J. Hsu, A. Kubetzka, A. Finco, N. Romming, K. Bergmann, and R. Wiesendanger, Nat. Nanotechnol. **12**, 123 (2017).

[75] Y. Liu, S. J. Xuan, M. Jia, and H. Yan, J. Phys. D: Appl. Phys. **50**, 48LT01 (2017).

[76] Y. Nakatani, M. Hayashi, S. Kanai, S. Fukami, and H. Ohno, Appl. Phys. Lett. **108**, 152403 (2016).

[77] G. Chen, A. Mascaraque, A. T. N'Diaye, and A. K. Schmid, Appl. Phys. Lett. **106**, 242404 (2015).

[78] L. Wang, C. Liu, N. Mehmood, G. Han, Y. Wang, X. Xu, C. Feng, Z. Hou, Y. Peng, X. Gao *et al.*, ACS Appl. Mater. Interfaces **11**, 12098 (2019).

[79] C. Moreau-Luchaire, C. Moutafis, N. Reyren, J. Sampaio, C. A. F. Vaz, N. Van Horne, K. Bouzehouane, K. Garcia, C. Deranlot, P. Warnicke *et al.*, Nat. Nanotechnol. **11**, 444 (2016).

[80] N. S. Gusev, A. V. Sadovnikov, S. A. Nikitov, M. V. Sapozhnikov, and O. G. Udalov, Phys. Rev. Lett. **124**, 157202 (2020).

[81] C. Baraduc, T. Srivastava, M. Schott, M. Belmeguenai, Y. Roussigné, A. Bernand-Mantel, L. Ranno, S. Pizzini, S. M. Chérif, A. Stashkevich *et al.*, Proc. SPIE **10732**, Spintronics XI, 1073232 (2018).

[82] C. Burrowes, N. Vernier, J. P. Adam, L. Herrera Diez, K. Garcia, I. Barisic, G. Agnus, S. Eimer, J. Kim, T. Devolder *et al.*, Appl. Phys. Lett. **103**, 182401 (2013).

[83] J. M. Winter, Phys. Rev. **124**, 452 (1961).

[84] W. Li, L. Zhao, and Z. Liu, Front. Mater. Sci. **13**, 323 (2019).

[85] D.-X. Chen, J. A. Brug, and R. B. Goldfarb, IEEE Trans. Magn. **27**, 3601 (1991).